



# Dynamic Recrystallization and Phase-Specific Corrosion Performance in a Super Duplex Stainless Steel

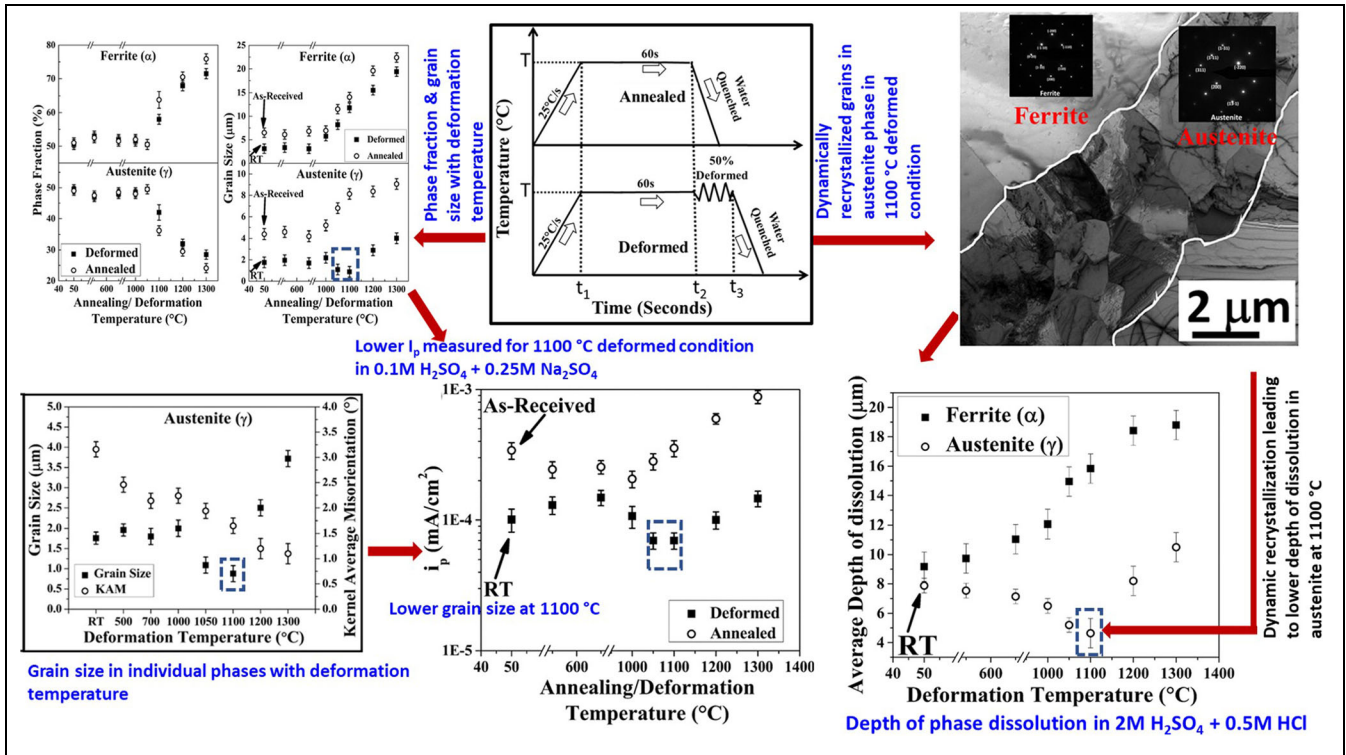
Riya Mondal, Sunil Kumar Bonagani, Parvej Raut, Saurabh Kumar, P.V. Sivaprasad, G. Chai, V. Kain, and I. Samajdar

Submitted: 23 March 2021 / Revised: 22 June 2021 / Accepted: 30 June 2021 / Published online: 21 September 2021

Super duplex stainless steel specimens were subjected to controlled (in a deformation simulator) thermal and thermal plus deformation treatments. The objective was to relate the corrosion performance with hot (1000–1300°C) deformed microstructures. The microstructural evolutions were quantified with extensive microtextural characterization and measurements of phase-specific micro-hardness. The corrosion behavior was investigated by anodic polarization and phase-specific selective dissolution methods. Though the thermal treatment imposed an increasing degradation in corrosion performance with holding temperature, the associated deformation at that temperature brought a non-monotonic behavior. The best corrosion performance (or the lowest passivation current density) was noted in the specimen deformed at ~1100°C. This superior corrosion behavior was attributed to the grain size refinement in the austenite phase. Finally, a combination of transmission Kikuchi diffraction (TKD) plus transmission electron microscopy (TEM) clearly related the grain size refinement to discontinuous dynamic recrystallization. The overall corrosion behavior was shown to be determined by a balance between decreasing austenite fraction and dynamic recrystallization-induced grain size refinement of the austenite phase.

Riya Mondal, Saurabh Kumar, and I. Samajdar, Department of Metallurgical Engineering & Materials Science, Indian Institute of Technology Bombay, Powai, Mumbai 400076, India; Sunil Kumar Bonagani and V. Kain, Materials Processing and Corrosion Engineering Division, Bhabha Atomic Research Centre, Trombay, Mumbai 400085, India; Parvej Raut, Department of Mechanical Engineering, Indian Institute of Technology Bombay, Powai, Mumbai 400076, India; P.V. Sivaprasad and G. Chai, Sandvik Materials Technology, SE- 811 81 Sandviken, Sweden. Contact e-mail: vivkain@barc.gov.in.

# Graphical Abstract



**Keywords** corrosion, duplex stainless steel, dynamic recrystallization, electron backscatter diffraction, hot deformation, microstructure

## 1. Introduction

Though the name ‘stainless’ was coined in 1913 for the first commercial chromium-bearing austenitic steel (Ref 1, 2), the duplex stainless steel (DSS) was commercialized only in 1930 (Ref 1–3). This interesting grade, having an almost equal presence of face-centered cubic (FCC) austenite and body-centered cubic (BCC) ferrite phases, offers properties and performance exceeding those of its single-phase counterparts (Ref 4). The developments in DSSs have been undertaken continuously in last ~90 years, (Ref 1, 2): starting from the original lean DSS or the first generation grade to more recent innovations of second and third generations—the super and the hyper grades. The classifications of DSS are primarily based on their resistance to pitting or pitting resistance equivalent number (PREN) (Ref 1). The alloy chemistry primarily determines the resistance to pitting of any DSS (Ref 1, 4, 5), but the substrate microstructure also plays a significant role in pitting as well as general corrosion resistance (Ref 6–9).

The high alloying element content and the high strength of the DSS naturally bring out fabrication challenges (Ref 1, 2,

10). Typically, such fabrication involves hot or hot plus cold working and the solutionizing heat treatment (Ref 11, 12). Even the last step, which simply requires heating and holding to a relatively high temperature, has interesting science and technology behind it. The solutionized DSS is water quenched immediately after the solutionizing to avoid the formation of harmful tertiary phases (Ref 1, 13, 14). The holding temperature and time of the solutionizing heat treatment determine the grain size plus phase fraction and phase-specific chemistry, and all these metallurgical parameters affect the corrosion resistance of SDSS (Ref 9). Similarly, the cold working (Ref 8, 15–17) and post-cold work annealing (Ref 18, 19) also affect the corrosion performance of SDSS because they control the presence of local lattice curvatures, i.e., local distortion in crystallographic orientation. It has been already reported, in a SDSS, that the presence of large lattice curvatures and associated high-angle grain boundaries were detrimental to the corrosion performance (Ref 8). At the same time, minor cold work did enhance the corrosion resistance.

With all such references relating to substrate microstructures with corrosion performance in DSS (Ref 6, 8, 9, 15–18), the hot working and associated microstructure evolution naturally become important. Controlled hot working, for example, has been successfully implemented to introduce superplastic deformation (Ref 20–22) or to produce micro-duplex structures (Ref 23), and, more relevant to the present study, to obtain optimized flow behavior (Ref 24–26). The latter, the basis of the processing maps (Ref 24, 27, 28) and numerous publications Ref 29–31 in DSS, is based on balancing between work

hardening and work softening. In particular, hot working is expected to produce reduced strain hardening than cold working. The relatively ‘subdued’ effect of high temperature plastic deformation is further softened by dynamic recovery (DRcv) and/or dynamic recrystallization (DRx). Dynamic recovery (Ref 32–34) is a high-temperature mechanism that evolves with a large deformation, in which immobile dislocations are released to annihilate immediately with neighboring dislocations of opposite sign. In dynamic recrystallization (opposed to static recrystallization), the nucleation and growth of new grains occur during high-temperature deformation itself (Ref 35–37). These are reported in hot working of DSS as well (Ref 38, 39).

However, how such evolution in hot worked and annealed microstructures would affect the corrosion performance of DSS has never been explored comprehensively. For example, in solution annealing treatment, both temperature and duration matter. G. Fargas et al. observed that the pitting resistance decreased with the decreasing of intermediate annealing temperature from 975°C to 875°C performed on cold-rolled DSS due to the formation of the undesired phases such as sigma phase at low annealing temperatures (Ref 40). M. Gholami et al. reported that the pitting corrosion resistance decreased with the increasing of solution annealing temperature with a preferential attack in the ferrite phase (Ref 41). X. Liu et al. also observed increased pitting corrosion resistance with the increasing of solution annealing temperature in the temperature range of 850–1100°C for SDSS (Ref 42). Similarly, several researchers have studied and discussed the effect of hot deformation on corrosion resistance of DSS. Y. H. Yang et al. reported that 2205 DSS, after deformation at 1050°C, showed deterioration in the pitting corrosion resistance. Deformation at this temperature favors dynamic recrystallization (DRX), which increases the  $\gamma/\gamma$  grain boundary and  $\delta/\gamma$  boundary (Ref 43). M. Dabala et al. proposed that the partial DRX of austenite, for example, after deformation at 950°C, improved the corrosion resistance of DSS (Ref 44). E. Paredes et al. stated that many useful products like corrugated bars are more prone to local corrosion, and fabrication through hot working provides better corrosion resistance (Ref 45). Even in large industrial forgings, hot deformation affects the pitting resistance (Ref 46).

The partitioning of austenite forming (Ni, N) and ferrite forming (Cr, Mo) elements with annealing temperature results in not only in different chemical compositions of the austenite and ferrite phase but also in differences in corrosion properties. The overall corrosion behavior of a DSS depends on the constituent ferrite and austenite phases. The microstructures of the constituent phases evolve differently with different hot deformation conditions; thus, the respective electrochemical corrosion behavior also changes in accordance with the changes in composition. Though some of these results provide great technological information, but details about microstructure and processing are still not adequate, and it is a matter of active research. Hot worked microstructure and its corrosion resistance thus provided the basis for this study. This is the

motivation behind the present study. This study correlates the microstructural developments such as grain size of phase-specific, misorientation and ferrite fraction that occurred during hot deformation of SDSS with the corrosion (passivation) behavior. The correlations between microtexture (grain refinement by dynamic recrystallization) and corrosion behavior (passivation) are first of its kind.

## 2. Experimental Procedure

### 2.1 Material and Processing

This study is on a SAF 2906 SDSS, and its chemical composition is listed in Table 1. Chemical composition was measured using optical emission spectroscopy (OES). It is to be noted that OES measurements were repeated twice and the average value is reported. The starting material (noted as as-received or AR) was received (from Sandvik™ Materials Technology, Sweden) as a hot-rolled and then solutionized (at 1050°C, 1 h) ~12-mm-thick plate. Though the microstructure appeared fully recrystallized, subsequent microtexture mea-

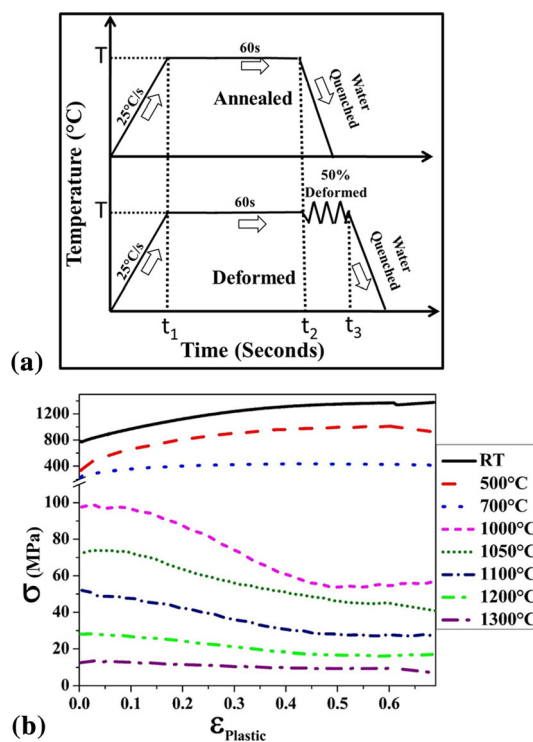


**Fig. 1** (a) Schematic of the thermal and thermal plus deformation treatments used in this study. For details on the temperature, refer to Table 2. (b) True plastic stress ( $\sigma$ ) versus true plastic strain ( $\epsilon_{\text{Plastic}}$ ) plots obtained from the compression tests in a deformation simulator at different temperatures

**Table 1** Composition of the super duplex stainless steel (Sandvik SAF-2906™) in weight %

Elements	C	Si	Mn	P	Cr	Ni	Mo	Cu	N	S
Weight %	0.03	0.30	1.01	0.015	29.05	7.02	2.30	0.80	0.35	0.012

**Table 2** Different temperatures used for the thermal and the thermal plus deformation cycles (as in Fig. 1)

Deformation temperature (50% plain strain compression)	Annealing temperature, without any deformation (holding time 60s)
Room temperature (RT) (27°C)	Not applicable
500°C	500°C
700°C	700°C
1000°C	1000°C
1050°C	1050°C
1100°C	1100°C
1200°C	1200°C
1300°C	1300°C

measurements showed signatures of ‘remnant’ plastic deformation and associated misorientation (Ref 47).

Cylindrical compression specimens of 8 mm diameter and 12 mm length were prepared from the mid-width and mid-thickness sections of the AR plate. As shown in Fig. 1a, two types of experiments were performed. One set of samples was subjected to controlled uniaxial compression in a deformation simulator (Gleeble3800<sup>TM</sup>) for different deformation temperatures (see Table 2). The compression tests were conducted to a 50% reduction in thickness (strain rate of 0.01 s<sup>-1</sup>), followed by water quenching. Figure 1b shows the flow behavior, a point discussed in the next section, of the corresponding compression tests. Further, another set of samples was subjected (see Fig. 1a) to the same (heating rate, holding temperature-time and water quenching) thermal treatment (but without imposing any deformation). Samples from the thermal tests provided the basis for easy comparison. Table 2 lists the temperatures for thermal and thermal plus deformation treatment used in this study. In this study, the thermal treatments are being referred to as annealing (without any deformation) although it is not annealing in the true sense.

## 2.2 Microstructural and Micro-hardness Characterizations of Specimens

Post-thermal and thermal plus deformation treatment, the specimens were sectioned (using electro-discharge machining), in two halves, parallel to the compression axis. Before the microstructural characterization, the surface of the specimens was polished metallographically, followed by a final electropolishing. For the latter, an electrolyte of 80:20 methyl alcohol and perchloric acid was used at -20°C and 16 volts dc. These were then subjected to microstructural characterization using electron backscattered diffraction (EBSD) with a TSL-OIM<sup>TM</sup> system in a FEI<sup>TM</sup> Quanta 3D-FEG (field emission gun) scanning electron microscope (SEM). For EBSD measurements, the beam, video and step sizes (0.3 μm) were kept identical. The specimens for transmission electron microscopy (TEM) were prepared by twin-jet polishing (Struers<sup>TM</sup> Tenupol-5) using the same electrolyte and electropolishing condition (as mentioned earlier for EBSD sample preparation). These were then examined by transmission kikuchi diffraction (TKD: using TSL-OIM<sup>TM</sup> system in a FEI<sup>TM</sup> Nova Nano SEM) and by TEM (Thermo<sup>TM</sup> Themis-300, operated at 300 keV).

Finally, Vickers micro-hardness measurements, of the respective phases, were made in a Fischerscope<sup>TM</sup> HM 2000.

At least 15 measurements were taken, for each phase in a specimen, with 10 mN load and 20 s dwell time.

## 2.3 Electrochemical Characterization

The electrochemical characterization of all the specimens was carried out by potentiodynamic and potentiostatic polarization. The test specimens were provided an appropriate electrical connection from one side while mounting in an epoxy resin to expose the opposite side of the specimen (at least 1 cm<sup>2</sup> area) to the electrolyte. The electrical connection wire was insulated to avoid contact with the test solution. For all the electrochemical measurements, the specimens were polished up to mirror finish with a diamond paste of 0.5 μm particle size and cleaned properly. The contact regions between the test specimen and the resin were covered with a nonconductive lacquer.

All the electrochemical tests were performed, as per ASTM G5 standard procedure, in a conventional three-electrode cell using a platinum foil as the auxiliary (counter) electrode, specimen as the working electrode and a saturated calomel electrode (SCE) as the reference electrode. The tests used a Bio-Logic<sup>TM</sup> VSP 300 potentiostat. The anodic polarization (passivation) behavior of deformed and thermal plus deformed conditions has been studied in the test solution of 0.1M H<sub>2</sub>SO<sub>4</sub> + 0.25 M Na<sub>2</sub>SO<sub>4</sub> at room temperature (25°C). At the start of each electrochemical experiment, the specimen was cathodically polarized at -1000 mV<sub>SCE</sub> for 60 s for surface cleaning, and this was followed by immersing in the solution for 30-45 min to obtain a stable open circuit potential (OCP). Argon gas was bubbled through the solution for 1 h before the start of electrochemical experiments to remove the dissolved oxygen and the bubbling was continued until the end of the experiment. A potential sweep with a scan rate of 10 mV/min was employed for the anodic polarization tests from -0.55 V<sub>SCE</sub> to 0.9 V<sub>SCE</sub>. The anodic polarization data (see Fig. 2a) were then analyzed, and passivation current density (i<sub>p</sub>) was measured as current density corresponding to the passive potential of 0.2 V<sub>SCE</sub>.

Further, to support the observed electrochemical results obtained in 0.1M H<sub>2</sub>SO<sub>4</sub> + 0.25 M Na<sub>2</sub>SO<sub>4</sub> solution, the hot-deformed specimens were subjected to selective dissolution of the ferrite and the austenite phases in 2 M H<sub>2</sub>SO<sub>4</sub> + 0.5 M HCl solution at 25°C. As mentioned, the focus of the present work is to explore the corrosion behavior of SDSS in hot-deformed conditions, these experiments were conducted only for hot-deformed conditions. For this, specimens mounted in epoxy

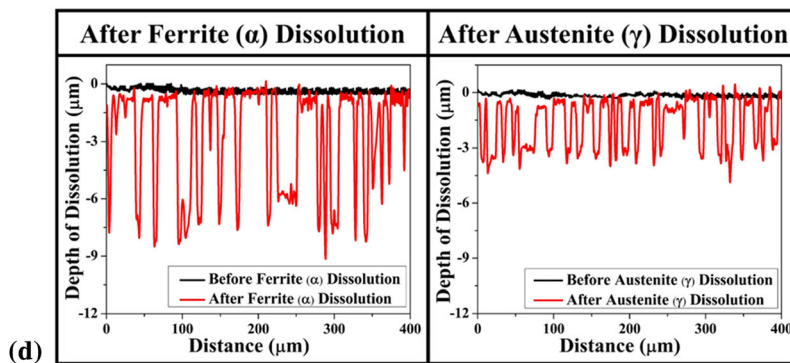
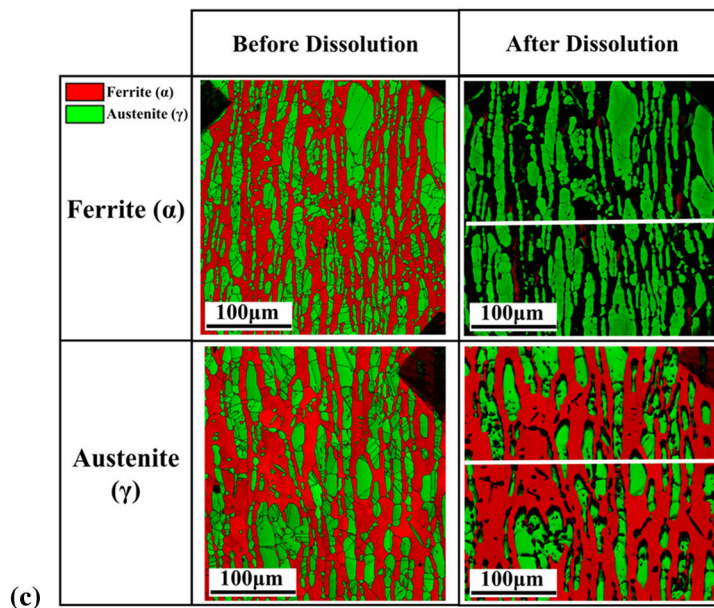
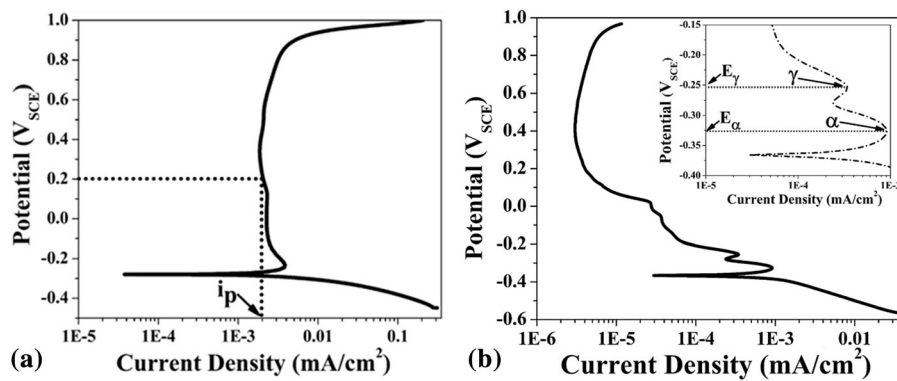


**Fig. 2** Typical anodic polarization curves (potential versus current density) in (a) 0.1M  $\text{H}_2\text{SO}_4 + 0.25\text{M Na}_2\text{SO}_4$  solution and (b) 2 M  $\text{H}_2\text{SO}_4 + 0.5\text{M HCl}$  solution. (a) also includes passivation current density ( $i_p$ ). The inset in Fig. 2(b) shows distinguishable ferrite ( $\alpha$ ) and austenite ( $\gamma$ ) dissolution peaks and their corresponding peak potentials. (c) Electron backscattered diffraction (EBSD) images (combining information on phase plus image quality IQ) showing selective dissolution in ferrite and austenite after phase-specific potentiostatic dissolution. (d) Depth of dissolution versus distance. These are shown, along the white lines marked in (c), respectively, for the ferrite ( $\alpha$ ) and the austenite ( $\gamma$ ) phases (before and after the dissolution for 1050°C)

resin (with appropriate electrical connections at the back) were suitably prepared (as mentioned earlier). First, potentiodynamic polarization tests (identical conditions as mentioned earlier) were conducted in an electrolyte of 2 M  $\text{H}_2\text{SO}_4 + 0.5\text{M HCl}$ . Two different anodic peaks were observed for the ferrite ( $\alpha$ ) and the austenite ( $\gamma$ ) phases (as shown in Fig. 2b). The  $i_p$  was measured at a passive potential of  $0.2V_{\text{SCE}}$ . Potentiostatic

polarization tests were conducted at these respective peak potential(s) ( $E_\gamma$  or  $E_\alpha$ , see Fig. 2b, for the respective phase(s)) in a freshly prepared solution 2 M  $\text{H}_2\text{SO}_4 + 0.5\text{M HCl}$  solution for 3 h to dissolve a particular phase. The methodology was otherwise identical to that earlier described for potentiodynamic polarization tests. The selective dissolution of the ferrite phase resulted in the formation of cavities and left the austenite phase

almost un-attacked (see Fig. 2c). The reverse was naturally valid for the selective dissolution of the austenite phase. The depth of dissolutions (see Fig. 2d) was quantified, for different phases and associated microstructure, by a 3-D non-contact optical profiler: Zeta™. It may be noted that the same electrolyte solution has been used for establishing the phase-specific peak potentials and its dissolution in the previous publications (Ref 8, 9, 19). Analytical reagent grade chemicals are used for preparing the solutions for conducting electrochemical corrosion experiments. Figure 2b-d illustrates the methodology used for (a) establishing the individual peak potentials for the ferrite and austenite phases, (b) direct observation of phase-specific dissolution after potentiostatic experiment and (c) depth of dissolution of post-selective phase dissolution.

### 3. Experimental Results

Figure 1b collates the results from the compression tests done at different deformation temperatures. It is clear that the effects of temperature on the flow stress and strain hardening were significantly different. For example, clear strain hardening was noted for compression tests done at room temperature (RT) and 500°C. For tests done at  $\geq 1000^\circ\text{C}$ , on the other hand, evidence of flow softening and flow saturation was observed (Fig. 1b). These different flow behaviors at different deformation temperature naturally reflected on the microstructural evolution. Microstructural evolution, as visualized through EBSD, for the entire range of thermal and thermal plus deformation cycles is collated in Fig. 3. More specifically, specimen deformed at RT and 500°C, showing clear strain

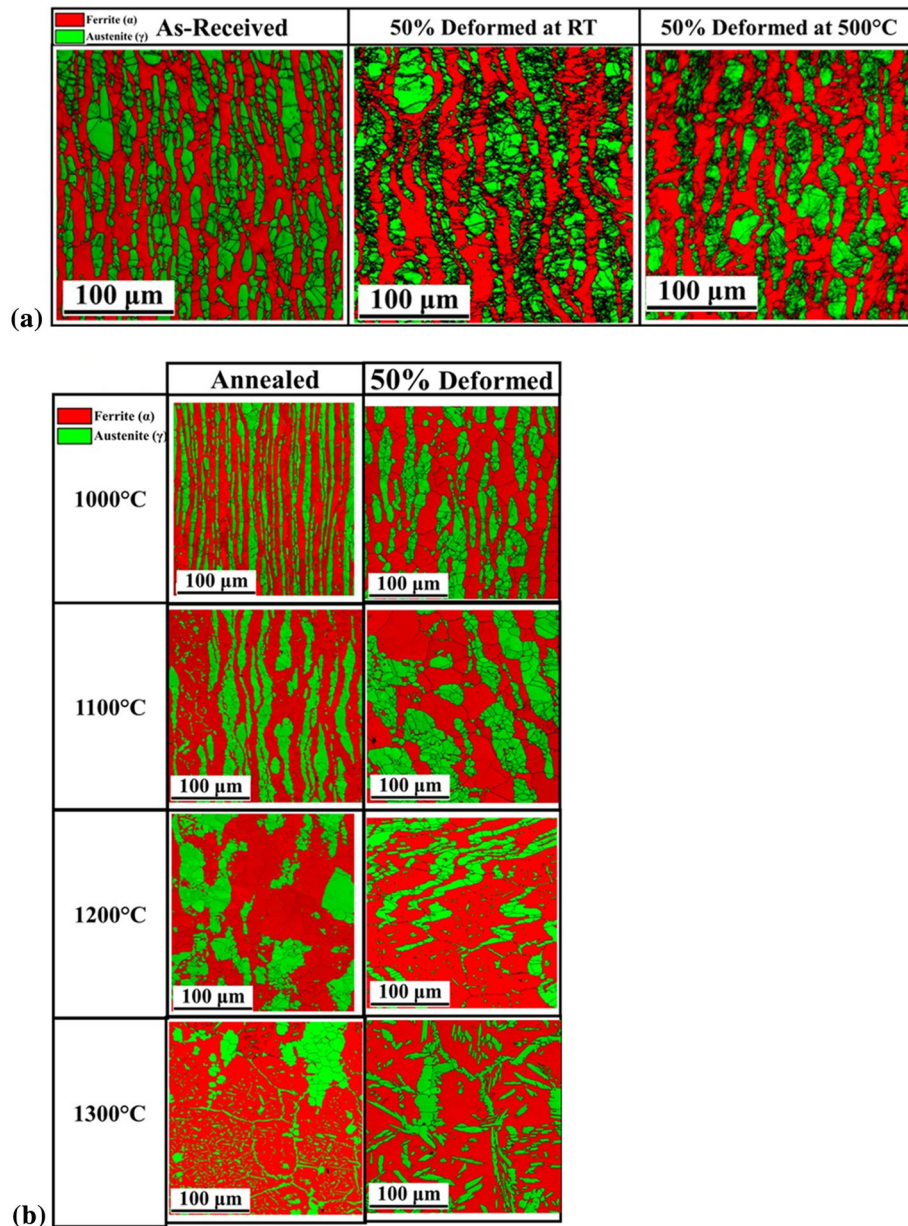


**Fig. 3** (a) EBSD image quality (IQ) plus phase maps of as-received (AR) SDSS and the AR 50% deformed at room temperature (RT) and at 500 °C. (b) Similar EBSD images are also shown for samples subjected to different thermal and thermal plus deformation treatments (Fig. 1 and Table 2)

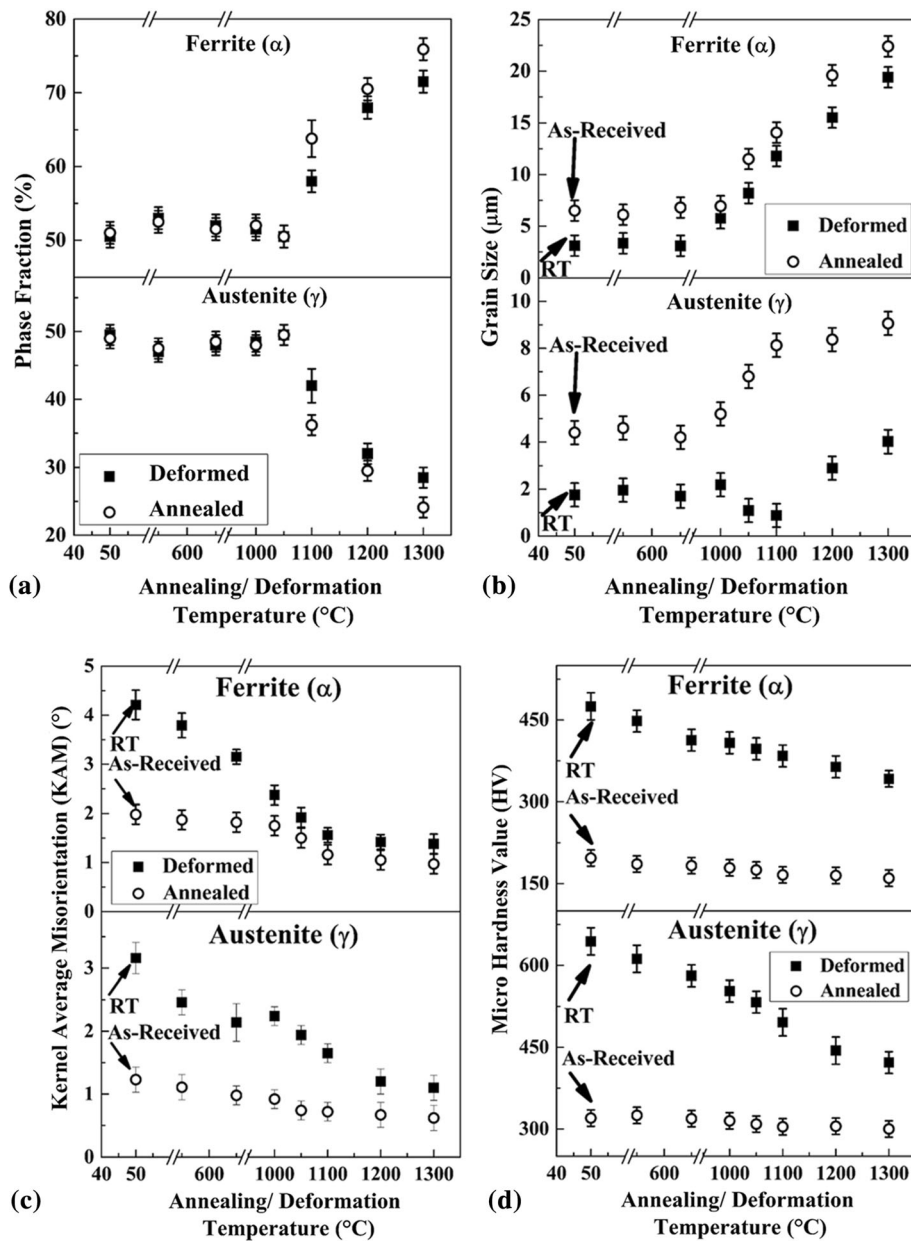


**Fig. 4** (a) Phase fraction, (b) grain size, (c) kernel average misorientation (KAM) and (d) micro-hardness for the ferrite ( $\alpha$ ) and the austenite ( $\gamma$ ) phases, in samples subjected to different thermal and thermal plus deformation treatments (for details refer: Fig. 1 and Table 2). In (a)-(d), error bars represent standard deviations from multiple measurements

hardening (as in Fig. 1b), is shown in Fig. 3a. It is to be noted that the thermal treatment at the same temperature (500°C) did not alter the microstructure. However, specimens subjected to both thermal and thermal plus deformation treatment above  $\geq 1000^\circ\text{C}$ , see Fig. 3b, brought out noticeable differences in the resultant microstructure. In particular, the phases appeared less strain hardened: an observation easily justified from the stress-strain behavior (Fig. 1b). Further, a qualitatively reduced fraction of the austenite phase with clear discontinuities (see Fig. 1b) was noted with an increase in temperature (in 1200°C and 1300°C). Absence of tertiary phases, like  $\text{Cr}_2\text{N}$  and sigma, was also confirmed on the water quenched samples by FEG-SEM. From Fig. 3b, it is clear that the annealing treatment above 1000°C changes the morphology of the two phases. The

thermal plus deformation treatment changes the morphology of the two phases at all the temperatures.

A quantitative comparison of the microstructural evolution is given in Fig. 4: in terms of phase fraction % (Fig. 4a) and phase-specific grain size (Fig. 4b), misorientation (Fig. 4c) and micro-hardness (Fig. 4d). The accurate phase identification was possible by considering a minimum of five Hough peaks (Ref 48–50) for the respective phase or space group. From such phase(s), average grain size and kernel average misorientation (KAM) values were then measured. It is to be noted that in an automated EBSD analysis, a grain was considered as a region bound by a continuous boundary with  $> 5^\circ$  misorientation. Such regions were ‘assumed’ as circular in shape, and grain size data from automated EBSD maps are often reported as the mean of the ‘circle equivalent diameters’ of the measured grain

areas and from that the average grain size was estimated. KAM, on the other hand, represented misorientation of every measurement point(s) with respect to its immediate neighbors (six—as a hexagonal grid was used in the present study), provided any such misorientation did not exceed 5°. Finally, a combination of EBSD plus micro-hardness enabled accurate measurements of phase-specific hardness.

Figure 3 and 4 brings out detailed comparative microstructural evolution between the two sets of samples, those produced by thermal and those produced by thermal plus deformation treatments (see Figure 1a and Table 2). As shown in Fig. 4a, > 1050°C treatments resulted in a near-monotonic increase in the transformation of austenite to ferrite. Further, the deformed specimens clearly showed a lower fraction of transformed ferrite. Though this study did not deliberate further on this interesting aspect of deformation-induced retardation of displacive phase transformation (Ref 51), this may be noted for future study and reference. Moreover, the microstructural evolution was not restricted only to the phase transformation. There were clear indications of phase-specific grain coarsening and even grain refinement (see Fig. 4b). The grain refinement

was observed only during 1000°C-1100°C deformation of the austenite phase, while hot-deformed austenite > 1100°C and ferrite > 700°C showed grain coarsening. On the other hand, appropriate thermal treatment (> 700°C for austenite ( $\gamma$ ) and > 1000°C for ferrite ( $\alpha$ )) led to clear grain coarsening. These, as will be presented later, constituted a critical aspect of the hot-deformed microstructure developments and had a significant implication for corrosion performance. Misorientation (see Fig. 4c), for all phases and conditions, showed a near-monotonic drop with an increase in temperature.

Of course, the drop in misorientation imposed by the thermal cycle was noticeably less (close to the measurement uncertainty, especially for the higher annealing temperatures) than the more significant decrease enabled by the higher temperature deformation. This point is further confirmed by the phase-specific micro-hardness measurements (Fig. 4d). As shown in Fig. 4d, the thermal cycle did not have a significant effect on the phase-specific hardness, but thermal plus deformation treatments provided clear softening (or decrease in hardness). In other words, high temperature deformation was

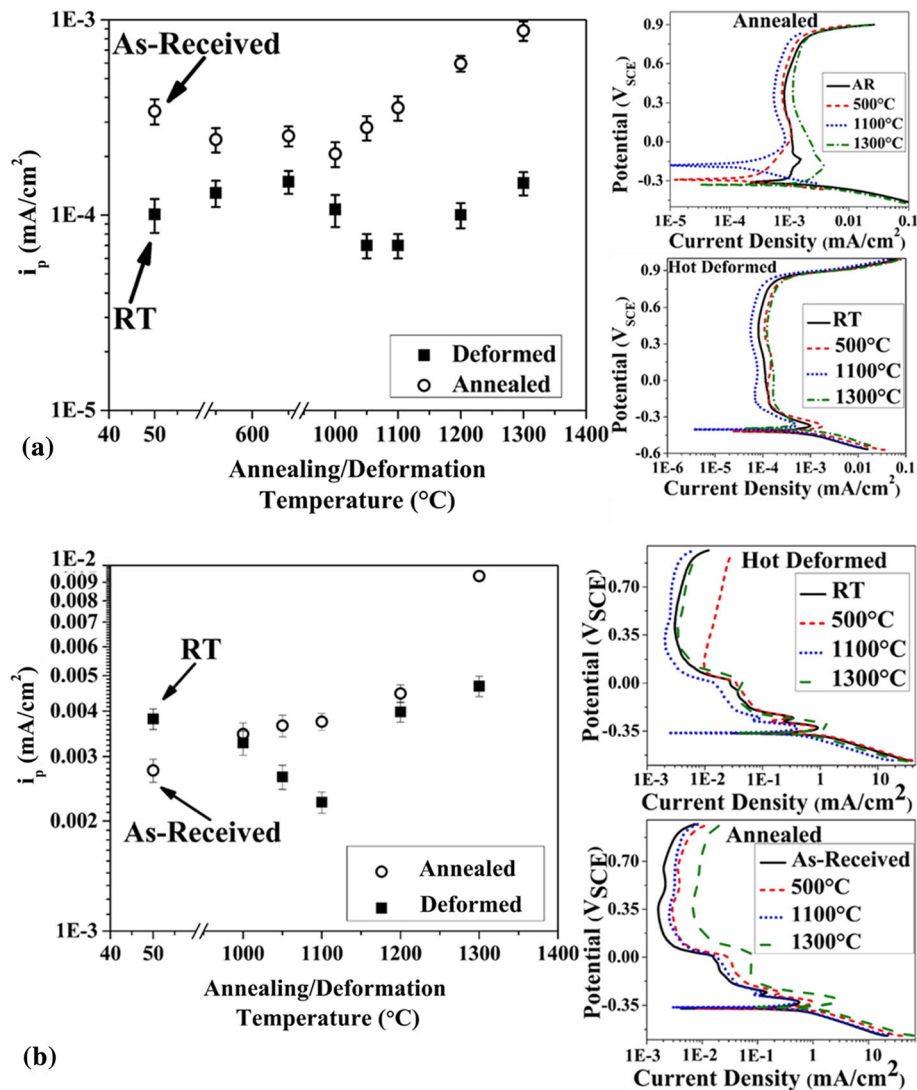


**Fig. 5** Estimated  $i_p$  (passivation current) values from anodic polarization data (selected plots are included) under (a) 0.1M  $H_2SO_4$  + 0.25M  $Na_2SO_4$  and (b) 2M  $H_2SO_4$  + 0.5M HCl. Error bars represent standard deviations from at least three anodic polarization tests



associated with significant softening. This, as presented subsequently, also affected the corrosion performance.

The passive current density ( $i_p$ ) values, as obtained from anodic polarization under two different electrolytes, are summarized in Fig. 5. In 0.1M  $H_2SO_4 + 0.25M Na_2SO_4$  solution, the studied conditions showed typical active-passive anodic polarization similar to anodic polarization observed for other stainless steels in  $H_2SO_4$  solution. The two activation peaks observed for SDSS in the solution of 2M  $H_2SO_4 + 0.5M HCl$  during anodic polarization were associated with selective dissolution of ferrite and austenite phases. This is mainly because of difference in the chemical composition of austenite and ferrite phases. It has been reported that the activation peak observed at lower potential region was associated with active dissolution of ferrite phase followed by its passivation, whereas austenite phase active dissolution occurred at higher potential region (Ref 53, 54). In this study, we have compared the effect of hot deformation temperature on the passivation behavior of SDSS. Since  $i_p$  values clearly reflect the extent of passivation (formation of  $Cr_2O_3$ ), these were used to represent the passivation behavior of the SDSS.  $I_{corr}$ , on the other hand, represents the corrosion rate at  $E_{corr}$ .  $I_{corr}$  may not be helpful in assessing the passivation characteristics at potentials higher (or more anodic) than  $E_{corr}$ , where passivity sets in. This is the reason that the present study, as well as previous publications from us on SDSS (Ref 8, 9, 19), used  $i_p$  values to define the corrosion performance of the SDSS. The  $i_p$ , estimated from 0.1M  $H_2SO_4 + 0.25M Na_2SO_4$ , covered the entire temperature range (Fig. 5a). For the annealed, or the samples subjected to only the thermal treatments, a slight increase in corrosion resistance (or decrease in  $i_p$ ) is observed till 1000°C, and this is followed by a clear increase in  $i_p$  (or decrease in passivity/corrosion resistance) at the higher temperatures. In contrast, the corrosion resistance of deformed specimens showed an interesting pattern (Fig. 5a): slight decrease (consistent, but well within the measurement uncertainty) till 700°C (i.e., increase in  $i_p$ ), a clear decrease from 700°C to 1100°C (i.e., decrease in  $i_p$ ) and a final degradation > 1100°C (i.e., increase in  $i_p$ ). This clear non-monotonic pattern for > 1000°C hot deformation cannot be explained by the near-monotonic increase (Fig. 4a) in the ferrite fraction or the relative softening (Fig. 4c and d).

Further, as the focus of the present study is in exploring the corrosion performance of the hot-deformed microstructures,  $i_p$  values and phase-specific dissolution were measured (for the relevant temperature range: RT plus 1000°C–1300°C) with 2M  $H_2SO_4 + 0.5M HCl$  electrolyte and a procedure explained earlier with Fig. 2. Figure 5b clearly shows a near-monotonic increase in  $i_p$  with annealing temperature versus a non-monotonic (lowest at 1100°C deformation) performance in hot-deformed specimens. Further exploration of the corrosion performance and its possible correlation with hot-deformed microstructures were attempted through microstructure-specific dissolution. The  $i_p$  values observed in the solution of 0.1M  $H_2SO_4 + 0.25M Na_2SO_4$  are one decade lower than the values observed in 2M  $H_2SO_4 + 0.5M HCl$  solution, and this is mainly due to the differences in the concentrations of the solutions. The lower concentration of  $H_2SO_4$  along with addition of  $Na_2SO_4$  decreased the general corrosion and also promoted the passivity in the studied conditions. The critical current density values observed in 2M  $H_2SO_4 + 0.5M HCl$  solution are almost three decades higher than the values observed in 0.1M  $H_2SO_4 + 0.25M Na_2SO_4$ . This is clearly the effect of chloride ions that

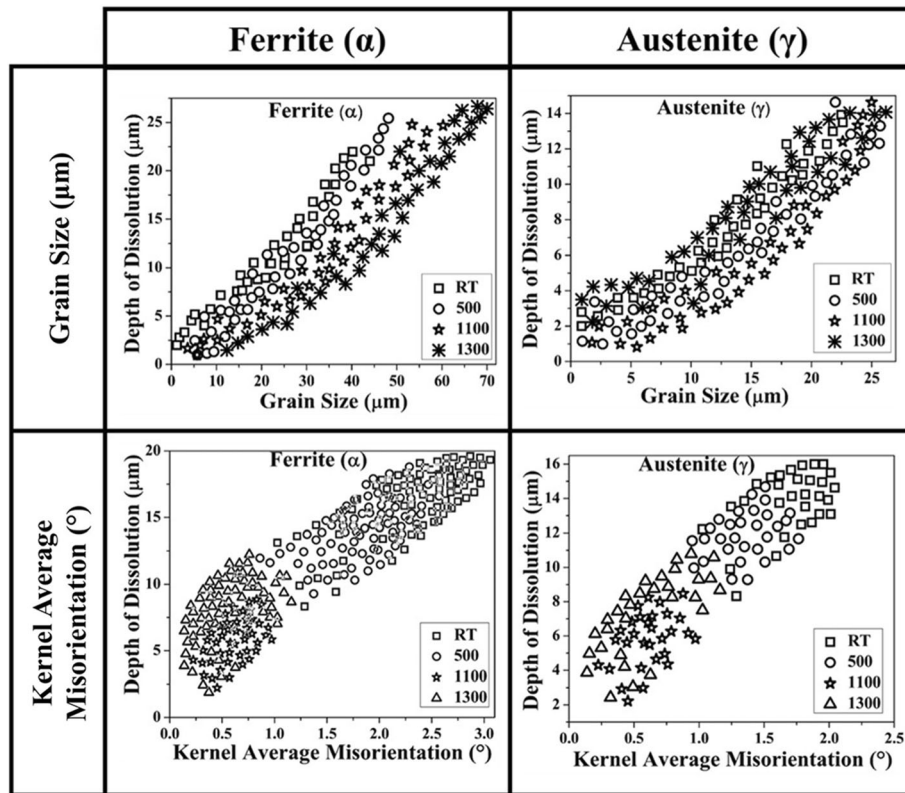
do not make the passive film as protective as in a non-chloride sulfate solution.

As shown in Fig. 6a (and all data are not included for brevity), depth of dissolution did scale with phase-specific grain size and KAM values. These naturally varied with deformation temperature. As shown in Fig. 6b—a monotonic increase in average depth of dissolution, with deformation temperature, is seen for the ferrite phase. In comparison, the austenite phase shows a non-monotonic pattern resembling the earlier trend in general corrosion (Fig. 5b). In brief, like the earlier studies on this SDSS grade (Ref 8, 9, 19), the patterns of general corrosion in 2M  $H_2SO_4 + 0.5M HCl$  (Fig. 5b) show a non-monotonic change in  $i_p$  with deformation temperature. The corrosion results were then extended to phase-specific dissolution under the same electrolyte (see Fig. 6b) showing the same non-monotonic behavior in the austenite phase. In brief, it appears that the austenite phase determined the general corrosion behavior of the two-phase alloy. In the two-phase SDSS, the austenite and the ferrite phases act as cathode and anode (Ref 53–55), respectively. Naturally, the galvanic corrosion behavior is important in such a two-phase metallic material. As indicated in a recent study (Ref 56), albeit on coarse pearlite, the galvanic corrosion and the local galvanic coupling depend on the phase boundary orientation relationship (OR). It may further be noted that the axis-angle nature of the austenite-ferrite phase boundary (Ref 9) did not change (these data are not included for brevity) noticeably with hot deformation. In other words, in the absence of changes in the galvanic coupling (Ref 56), between the austenite and the ferrite phases, it appeared that the corrosion performance of the SDSS grade was decided by the microstructural evolution in the respective phases.

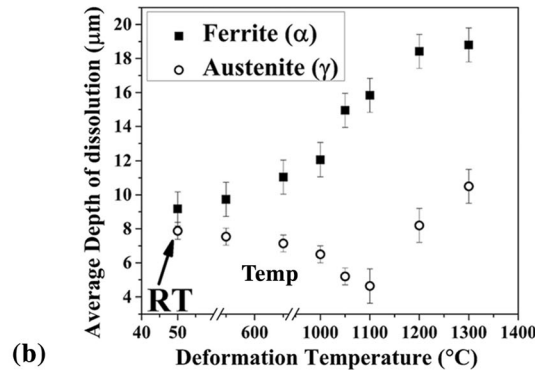
As summarized in Fig. 7a, the hot deformation temperature brings an increase in grain size and a reduction in KAM for the ferrite phase. Though the austenite showed a reduction in KAM, there was clear non-monotonic change in grain size: grain refinement from 1000°C to 1100°C followed by grain coarsening > 1100°C. The relative effects of grain size and KAM (Fig. 7a) on the respective phases are further decoupled in Fig. 7b (for ferrite) and Fig. 7c (for austenite). These showed the same trend: corrosion resistance, for both phases, reduced (i.e., more depth of dissolution) with grain coarsening but increased (i.e., lesser depth of dissolution) with relative softening (and decrease in KAM). KAM is a result of strain localization. The strain distribution was estimated using the KAM parameter measured by EBSD. Increase in KAM indicates high strain concentration, which affects the corrosion performance (protectiveness of the passive film). In brief, it is apparent that the non-monotonic corrosion performance of the SDSS, in general (Fig. 5b), and in particular, for the austenite phase (Fig. 6b) was enabled by the deformation-induced grain size refinement in the austenite. As the grain refinement was the highest for deformation at 1100°C (Fig. 7a), this was naturally the working temperature for the best corrosion resistant SDSS grade. The grain size refinement, during austenite hot working, is the focus of the next section in discussion.

## 4. Discussion

Fabrication of metallic materials, including two-phase DSS (Ref 2), always involves hot working (Ref 1, 5). Any classical review or textbook on hot working describes it firstly in terms



(a)



(b)

**Fig. 6** (a) The correlation of the grain size and kernel average misorientation (KAM) of ferrite and austenite phases with depth of dissolution in the electrochemical potentiostatic test. These are shown from samples subjected to various thermal plus deformation treatments. (b) Average depth of dissolution for each phase versus deformation temperature for ferrite and austenite phases. Error bars represent standard deviation of the experimental data (on depth of dissolution)

of the stress–strain response. For example, cold working is reflected in the work hardening, while hot working often involves work softening (Ref 51). The latter may include a simple flow saturation representing dynamic recovery (DRcv), or a drop in stress and inflection in the stress–strain response (Ref 25, 57–59) signifying dynamic recrystallization (DRx). The onset of discontinuous DRx in metallic materials, for example—in FCC copper and austenitic iron (Ref 60–62)—was observed before peak stress followed by a clear inflection or softening. However, in non-cubic hexagonal zirconium (Ref 63), the discontinuous DRx was noted without an inflection. Thool et al. Ref 63 tried to relate this analytically with three factors: DRx being ‘limited’ in (i) grain size and (ii) kinetics, plus (iii) extensive dynamic recovery. It is to be noted that the present SDSS revealed only flow saturation (Fig. 1b) repre-

sented dynamic recovery, while EBSD showed clear evidence of grain refinement (Fig. 3b), symbolizing dynamic recrystallization. Further, austenite-to-ferrite phase transformation alone, as evident in the samples subjected to only the thermal treatments (Fig. 4a), enabled clear grain coarsening (Fig. 4b). In brief, indirect experimental evidence on grain coarsening, in samples undergoing phase transformation, versus grain refinement, in samples subjected to thermal plus deformation treatments, strongly indicates DRx as the mechanism behind the observed grain refinement in the hot-deformed austenite phase.

It is important, at this stage, to review the available literature on DRx and DRcv in DSS (Ref 32, 34, 38, 64–67). Arguably, such references are contradictory at times. For example, Cizek and Wynne in 1997 reported (Ref 32) the absence of DRx in the

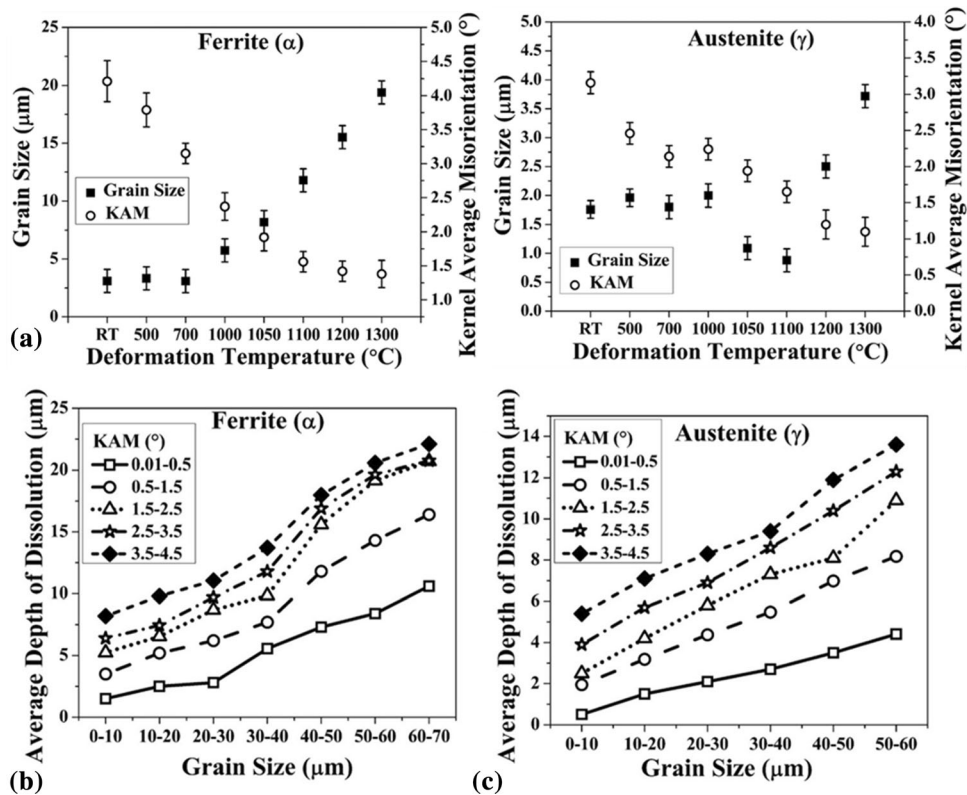


**Fig. 7** Average (a) grain size and kernel average misorientation (KAM), for different deformation temperatures, of the ferrite and the austenite phase. In (a), error bars represent standard deviations from multiple EBSD scans. Average depth of dissolution versus grain size for (b) ferrite and (c) austenite phases, respectively. In (b) and (c), the data (as in Fig. 5a, and more) were subjected to appropriate binning, for grain size and KAM, and then plotted

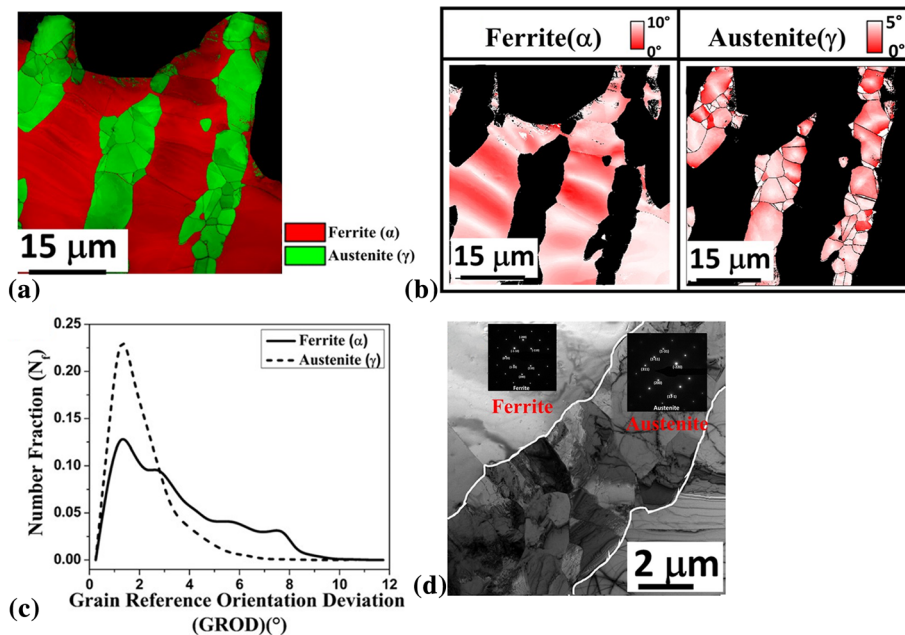


**Fig. 8** (a) Phase and (b) grain reference orientation deviation (GROD) maps of 1100 °C deformed specimen, as obtained from transmission Kikuchi diffraction (TKD). (c) Number fraction versus GROD for ferrite and austenite phase. (d) Bright field transmission electron microscopy (and associated micro-diffraction patterns) showing both phases, and dynamically recrystallized grains in the austenite phase

ferrite phase. On the other hand, Fan et al. Ref 68, in 2009—based purely on optical microscopy—claimed DRx in the ferrite phase. Iza-Mendia et al. Ref 38 explored DSS, both

cast and wrought, hot working with excellent SEM channeling contrast plus TEM imaging. They proposed that DRx has been suppressed in the austenite phase. However, a large body of

**Table 3 Relevant (to hot working) microstructural inputs ( $M_{Input}$ ), and their relationship with deformation temperature ( $T_{Def}$ ) and corrosion resistance ( $C_R$ ). A summary of corrosion resistance with  $T_{Def}$ , with respect to the relevant  $M_{Input}$ , is then given.**

Microstructural input ( $M_{Input}$ )	$M_{Input} = f(T_{Def})$	Corrosion resistance ( $C_R$ ) = $f(M_{Input})$
Ferrite fraction ( $F_\alpha$ )	$F_\alpha \propto T_{Def}$	$C_R \propto 1/F_\alpha$
Average grain size:	$d_{av}^z \propto T_{Def}$ , for all $T_{Def}$	$C_R^z \propto (\frac{1}{d_{av}^z})$
Ferrite ( $d_{av}^f$ )	$d_{av}^f \propto T_{Def}$ , unless there is a DRx	$C_R^f \propto (\frac{1}{d_{av}^f})$
Austenite ( $d_{av}^a$ )		
Misorientation ( $\Delta\theta$ )	$\Delta\theta \propto 1/T_{Def}$	$C_R \propto \Delta\theta$
Summary: $\Delta\theta$ drop is often minor. Corrosion resistance is thus expected to reduce with $T_{Def}$ , unless there is a grain size refinement by DRx.		

published literature (see Evangelista et al. Ref 69, Dehghan-Manshadi and Hodgson Ref 37, Fan et al. Ref 68, Cizek Ref 33, Haghdadi et al. Ref 70, Kingklang and Uthaisangskuk Ref 39) clearly indicated discontinuous DRx in the austenite phase. It has been reported (Ref 40) that DRx grain size in the austenite phase is 1/3rd of that of austenitic steels under identical deformation conditions, and the DRx happened (Ref 69) only at very high temperature. This plus the excellent dynamic recovery naturally makes (Ref 63) the present SDSS grade prone to exhibit flow softening instead to more classical DRx-induced inflection.

Experimental difficulties in exploring DRx-induced microstructural evolution are (i) avoiding post-hot deformation static recrystallization, and (ii) accurate microstructural characterization. These were addressed in the present study by using a deformation simulator (with appropriate water quenching—a cooling rate of  $\sim 550^\circ\text{C/s}$  being reported (Ref 71) on the specimen surface) and a combination of transmission kink diffraction (TKD) plus transmission electron microscopy (TEM), see Fig. 8. The TKD (Fig. 8a), for example, clearly captured a few large ferrite grains and much smaller austenite grains, in clusters, in the  $1100^\circ\text{C}$  deformed plus quenched microstructure. The orientation gradients inside a grain can be represented as grain reference orientation deviation or GROD. The GROD represents the misorientation of every measurement point within a grain with respect to the grain average (quaternion average) orientation. The GROD thus can be a true measure of the orientation gradients inside a grain. The TKD, on the other hand, is extremely effective in capturing very small misorientations at excellent spatial resolution. Naturally, TKD based GROD was shown (Ref 63) to be extremely effective in capturing signatures of plastic deformation (in general) and, in particular, the DRx grains. The same technique has been adopted in the present study as well. As shown in Fig. 8b, orientation gradients, or GROD, were observed in both austenite and ferrite grains. Though such orientation gradients were noticeably more in the larger ferrite grains (Fig. 8c), the smaller austenite grains showed clear presence of dislocation substructures inside the grains (Fig. 8d). In other words, both recrystallization and plastic deformation were involved in the creation of smaller austenite grains: establishing clearly DRx as the mechanism for the grain size refinement in the austenite phase.

There are numerous studies on hot working in DSS (Ref 45, 46, 72). Arguably, these are, at times, inconsistent. Part of this can be attributed to the different grades and starting microstructures of DSS: cast versus wrought, and lean versus super and

hyper. For example, this study is specific to SDSS SAF 2906, which is scientifically and technologically important. However, it is unknown if observations on DRx during hot working in wrought SAF 2906 can be translated to other grades and starting microstructures. Therefore, the real contribution of this study was to quantitatively define the role of deformation temperature on the microstructural evolution and then to link the relevant microstructural parameters (from hot working) to the corrosion performance. These naturally constitute a broader topic, which is expected to be grade independent and novel.

Paredes et al. Ref 45, for example, explored corrosion performance of hot and cold worked corrugated austenitic and DSS rebars. They found that surfaces of the corrugated bars are more prone to local corrosion, and fabrication through hot working provided better corrosion resistance. Such a study is of clear technological relevance but lacks any details on microstructure or processing. Ciuffini et al.'s Ref 46 observation that 'thermal history coupled with plastic deformation decides resistance to pitting corrosion' is categorical, and they even attempted some correlation with optical microstructures of large industrial forgings. However, identification of the relevant microstructural parameters appears inadequate in their study. There are also clear contradictions. Scupira et al. Ref 72 proposed better corrosion resistance in warm-rolled DSS, while Seshweni et al. Ref 73 claimed cold rolling to be better. In the absence of appropriate microstructural inputs and understanding, such contradictions are expected. It is to be noted that the corrosion performance for the present grade of SDSS shows non-monotonic behavior with imposed strain (Ref 8) and also with deformation temperature (Fig. 5b). Such non-monotonic behavior, even with a single process parameter, has an explanation in the form of interplay between different microstructural inputs. Without identifying the appropriate microstructural inputs and their relative role on corrosion performance, any experimental study is bound to be very subjective. The present study tries to bring some objectivity into this. Firstly, it identified the relevant (for hot working) microstructural parameters: phase fraction, grain size and misorientation. These microstructural inputs ( $M_{Input}$ ) were then related, experimentally, to the deformation temperature ( $T_{Def}$ ) and the corrosion resistance ( $C_R$ ), see Table 3. Table 3 also brings out the natural conclusion of this study: corrosion resistance is expected to reduce with increasing  $T_{Def}$ , unless there is a grain size refinement by DRx. This conclusion is expected to be grade independent and appears to be the primary contribution of this study.

## 5. Conclusions

This study explored quantitative microstructural evolution in SDSS, SAF 2906, through controlled thermal and thermal plus deformation treatments. Relevant microstructural parameters from hot working were then related to the corrosion resistance. The following are the main conclusions:

- At temperature of deformation  $\leq 1000^{\circ}\text{C}$ , SDSS showed strain hardening while flow saturation was observed at deformation temperature  $\geq 1000^{\circ}\text{C}$ . However, no inflection in the work hardening response, the classical signature of discontinuous dynamic recrystallization (DRx), was noted at temperatures  $\geq 1000^{\circ}\text{C}$ .
- Annealing (from thermal treatments) and deformation (from thermal and deformation treatments) brought the following microstructural responses:
  - At temperatures  $\geq 1050^{\circ}\text{C}$ —increase in austenite-to-ferrite phase transformation occurred in both annealing treatments and annealing plus deformation treatments. However, the extent of phase transformation is slightly less with the introduction of deformation.
  - At temperature  $\geq 1000^{\circ}\text{C}$ —grain coarsening of both ferrite and austenite phases occurred with thermal treatments. Thermal plus deformation treatments also produced grain coarsening of ferrite. However, clear grain refinement was observed, between  $1000^{\circ}\text{C}$  and  $1100^{\circ}\text{C}$  deformation, in the austenite phase.
  - Softening, as estimated by misorientation, was observed in in both phases with annealing and thermal plus deformation treatments. The softening through thermal treatments was, however, insignificant as compared to thermal plus deformation treatments.
- At temperatures  $\geq 1000^{\circ}\text{C}$  – corrosion resistance of the SDSS increased (i.e.,  $i_p$  decreased) near-monotonically with annealing temperature. However, a non-monotonic response was observed in the hot-deformed specimens: increase in  $i_p$  at deformation temperatures  $1000^{\circ}\text{C}$ – $1100^{\circ}\text{C}$  followed by a decrease at higher deformation temperatures. A similar pattern of non-monotonic corrosion resistance response was also noted for the austenite phase.
- It was shown that phase-specific corrosion resistance increased (i.e.,  $i_p$  decreased) with grain refinement and with enhanced softening (or decrease in misorientation). Thus, the non-monotonic corrosion resistance, with deformation temperature, was clearly related to grain refinement, during deformation at  $1000^{\circ}\text{C}$ – $1100^{\circ}\text{C}$ , in the austenite phase.
- A combination of transmission Kikuchi diffraction plus transmission electron microscopy clearly identified DRx as the mechanism behind grain refinement in the austenite phase. As the DRx was ‘limited’ in grain size and kinetics and microstructure was associated with extensive dynamic recovery, the DRx did not create classical inflection in the stress-strain response.
- In DSS, corrosion resistance is shown to reduce with deformation temperature,  $T_{\text{Def}}$ , unless there is a grain size refinement by DRx.

## Acknowledgment

The authors would like to acknowledge support from Sandvik™ Materials Technology, Sweden and CoEST (center of excellence on steel technology, IIT Bombay). Support from the National Facility of Texture and OIM (IIT Bombay) is also appreciated.

## Data Availability

The raw data required to reproduce the results of the present manuscript cannot be shared at this time as the data also form part of ongoing doctoral work.

## References

1. R. Gunn, *Duplex Stainless Steels: Microstructure, Properties and Applications*, Elsevier, England, Cambridge, 1997
2. I.M. Association, Practical guidelines for the fabrication of duplex stainless steels, **2009**, p 1-64, London, UK, [https://www.imoa.info/download\\_files/stainlesssteel/Duplex\\_Stainless\\_Steel\\_3rd\\_Edition.pdf](https://www.imoa.info/download_files/stainlesssteel/Duplex_Stainless_Steel_3rd_Edition.pdf)
3. J. Charles, Duplex stainless steels, a review after DSS'07 in Grado, *Revue de Métallurgie– Int. J. Metall.*, 2008, **105**(3), p 155–171.
4. J. Olsson and M. Snis, Duplex—a new generation of stainless steels for desalination plants, *Desalination*, 2007, **205**(1–3), p 104–113.
5. J.O. Nilsson, Super duplex stainless steels, *Mater. Sci. Technol.*, 1992, **8**(8), p 685–700.
6. L. Jinlong, L. Tongxiang, W. Chen and D. Limin, Comparison of corrosion properties of passive films formed on coarse grained and ultrafine grained AISI 2205 duplex stainless steels, *J. Electroanal. Chem.*, 2015, **757**, p 263–269.
7. L. Jinlong, L. Tongxiang, W. Chen and D. Limin, Effect of ultrafine grain on tensile behaviour and corrosion resistance of the duplex stainless steel, *Mater. Sci. Eng. C*, 2016, **62**, p 558–563.
8. R. Mondal, S.K. Bonagani, A. Lodh, T. Sharma, P. Sivaprasad, G. Chai, V. Kain and I. Samajdar, Relating general and phase specific corrosion in a super duplex stainless steel with phase specific microstructure evolution, *Corrosion*, 2019, **75**(11), p 1315–1326.
9. R. Mondal, A. Rajagopal, S.K. Bonagani, A. Prakash, D. Fuloria, P. Sivaprasad, G. Chai, V. Kain and I. Samajdar, Solution annealing of super duplex stainless steel: correlating corrosion performance with grain size and phase-specific chemistry, *Metall. Mater. Trans. A*, 2020, **51**, p 2480–2494.
10. I. Alvarez-Armas and S. Degallaix-Moreuil, *Duplex Stainless Steels*, Wiley, London, 2013
11. J. Cabrera, A. Mateo, L. Llanes, J. Prado and M. Anglada, Hot deformation of duplex stainless steels, *J. Mater. Process. Technol.*, 2003, **143**, p 321–325.
12. T.A. Debold, Duplex stainless steel—microstructure and properties, *JOM*, 1989, **41**(3), p 12–15.
13. H.D. Solomon, T. Devine Jr, Duplex stainless steels—a tale of two phases, in: *Duplex stainless steels*, 1982, pp. 693–756
14. M. Rosso, I. Peter and D. Suani, About heat treatment and properties of duplex stainless steels, *J. Achiev. Mater. Manuf. Eng.*, 2013, **59**, p 26–36.
15. K. Takizawa, Y. Shimizu, Y. Higuchi and I. Tamura, Effect of cold work and volume fraction of ferrite on corrosion resistance of ( $\alpha$ - $\gamma$ ) duplex stainless steel, *Tetsu-to-Hagane*, 1983, **69**(11), p 1448–1455.
16. A. Elhoud, H. Ezuber and W. Deans, Influence of cold work and sigma phase on the pitting corrosion behavior of 25 chromium super duplex stainless steel in 3.5% sodium chloride solution, *Mater. Corros.*, 2010, **61**(3), p 199–204.
17. M. Breda, K. Brunelli, F. Grazzi, A. Scherillo and I. Calliari, Effects of cold rolling and strain-induced martensite formation in a SAF 2205 duplex stainless steel, *Metall. Mater. Trans. A*, 2015, **46**(2), p 577–586.
18. A. Elhoud, N.C. Renton and W.F. Deans, The effect of manufacturing variables on the corrosion resistance of a super duplex stainless steel, *Int. J. Adv. Manuf. Tech.*, 2011, **52**(5–8), p 451–461.
19. R. Mondal, S.K. Bonagani, P. Raut, P. Sivaprasad, G. Chai, V. Kain and I. Samajdar, Role of recovery and recrystallization on the post cold work corrosion performance in a super duplex stainless steel, *J. Electrochem. Soc.*, 2020, **167**, p 101501.

20. K. Tsuzaki, H. Matsuyama, M. Nagao and T. Maki, High-strain rate superplasticity and role of dynamic recrystallization in a superplastic duplex stainless steel, *Mater. Trans. JIM*, 1990, **31**(11), p 983–994.
21. J. Li, X. Ren and X. Gao, Effect of superplastic deformation on microstructure evolution of 3207 duplex stainless steel, *Mater. Character.*, 2020, **164**, p 110320.
22. K. Osada, S. Uekoh and K. Ebato, Superplasticity of as rolled duplex stainless steel, *Tran. I. S. Ins. Japan/Tetsu-To-Hagane*, 1987, **27**(9), p 713–718.
23. S. Sasaki, T. Katsumura and J. Yanagimoto, Grain refinement technology for duplex stainless steel using rapid cooling immediately before hot working, *J. Mater. Process. Technol.*, 2020, **281**, p 116614.
24. H. Alinejad, B. Koroji, G. Ebrahimi and A. Momeni, Microstructure and flow behavior of cast 2304 duplex stainless steel at elevated temperatures, *J. Mater. Res.*, 2016, **31**, p 3939–3947.
25. Y. Han, D. Zou, Z. Chen, G. Fan and W. Zhang, Investigation on hot deformation behavior of 00Cr23Ni4N duplex stainless steel under medium–high strain rates, *Mater. Charact.*, 2011, **62**, p 198–203.
26. S. Spigarelli, M. El Mehtedi, P. Ricci and C. Mapelli, Constitutive equations for prediction of the flow behaviour of duplex stainless steels, *Mater. Sci. Eng. A*, 2010, **527**(16–17), p 4218–4228.
27. G. Fargas, N. Akdut, M. Anglada and A. Mateo, Microstructural evolution during industrial rolling of a duplex stainless steel, *ISIJ Int.*, 2008, **48**(11), p 1596–1602.
28. A. Momeni and K. Dehghani, Hot working behavior of 2205 austenite–ferrite duplex stainless steel characterized by constitutive equations and processing maps, *Mater. Sci. Eng. A*, 2011, **528**(3), p 1448–1454.
29. O. Balancin, W. Hoffmann and J. Jonas, Influence of microstructure on the flow behavior of duplex stainless steels at high temperatures, *Metall. Mater. Trans. A*, 2000, **31**(5), p 1353–1364.
30. L. Chen, X. Ma, X. Liu and L. Wang, Processing map for hot working characteristics of a wrought 2205 duplex stainless steel, *Mater. Des.*, 2011, **32**(3), p 1292–1297.
31. D. Rajabi, A. Abedi and G. Ebrahimi, Study on static recrystallization process in duplex stainless steel, *IJSS*, 2011, **8**, p 20–23.
32. P. Cizek and B. Wynne, A mechanism of ferrite softening in a duplex stainless steel deformed in hot torsion, *Mater. Sci. Eng. A*, 1997, **230**(1–10), p 88–94.
33. P. Cizek, The microstructure evolution and softening processes during high-temperature deformation of a 21Cr–10Ni–3Mo duplex stainless steel, *Acta Mater.*, 2016, **106**(1–2), p 129–143.
34. N. Haghdadadi, P. Cizek, H. Beladi and P.D. Hodgson, The austenite microstructure evolution in a duplex stainless steel subjected to hot deformation, *Philos. Mag.*, 2017, **97**(15), p 1209–1237.
35. W. Chen, C. Zheng, C. Jia, B. Hu and D. Li, Strain-rate dependence of the dynamic softening in a duplex stainless steel, *Mater. Character.*, 2020, **162**, p 110219.
36. N. Haghdadadi, P. Cizek, H. Beladi and P. Hodgson, A novel high-strain-rate ferrite dynamic softening mechanism facilitated by the interphase in the austenite/ferrite microstructure, *Acta Mater.*, 2017, **126**, p 44–57.
37. A. Dehghan-Manshadi and P. Hodgson, Effect of  $\delta$ -ferrite co-existence on hot deformation and recrystallization of austenite, *J. Mater. Sci.*, 2008, **43**(18), p 6272–6277.
38. A. Iza-Mendia, A. Pinol-Juez, J. Urcola and I. Gutierrez, Microstructural and mechanical behavior of a duplex stainless steel under hot working conditions, *Metall. Mater. Trans. A*, 1998, **29**(12), p 2975–2986.
39. S. Kingklang and V. Uthaisangskul, Investigation of hot deformation behavior of duplex stainless steel grade 2507, *Metall. Mater. Trans. A*, 2017, **48**(1), p 95–108.
40. G. Fargas, M. Anglada and A. Mateo, Effect of the annealing temperature on the mechanical properties, formability and corrosion resistance of hot-rolled duplex stainless steel, *J. Mater. Process. Technol.*, 2009, **209**(4), p 1770–1782.
41. M. Gholami, M. Hoseinpoor and M.H. Moayed, A statistical study on the effect of annealing temperature on pitting corrosion resistance of 2205 duplex stainless steel, *Corr. Sci.*, 2015, **94**, p 156–164.
42. X. Liu, C. Zhang, J. Li, W. Chen, Y. Zheng, H. Li and P. Han, Effect of solution annealing on microstructure evolution and pitting corrosion resistance of SAF2906 super duplex stainless steel, *Steel Res. Int.*, 2017, **88**(11), p 1700023.
43. Y.H. Yang and S.H. Li, High temperature deformation behavior and corrosion resistance of 2205 duplex stainless steel under strain rate of 0.5 s<sup>-1</sup>, *Adv. Mater. Res. Trans. Tech. Publ.*, 2012, **581**, p 1054–1057.
44. M. Dabala, I. Calliari and A. Variola, Corrosion behavior of a superduplex stainless steel in chloride aqueous solution, *J. Mater. Eng. Perform.*, 2004, **13**(2), p 237–240.
45. E. Paredes, A. Bautista, S.M. Álvarez and F. Velasco, Influence of the forming process of corrugated stainless steels on their corrosion behaviour in simulated pore solutions, *Corr. Sci.*, 2012, **58**, p 52–61.
46. A.F. Ciuffini, S. Barella, C. Di Cecca, A. Gruttadauria, S. Crugnola and C. Mapelli, Local pitting corrosion resistance evaluation in large forged UNS-S32760 super duplex stainless steel parts of a sphere valve for the oil & gas industry, *Metall. Ital.*, 2017, **10**, p 33–45.
47. S.I. Wright, M.M. Nowell, R. De Kloe and L. Chan, Orientation precision of electron backscatter diffraction measurements near grain boundaries, *Microsc. Microanal.*, 2014, **20**(3), p 852–863.
48. P.J. Goodhew and J. Humphreys, *Electron Microscopy and Analysis*, CRC Press, London, 2000
49. S.I. Wright, A review of automated orientation imaging microscopy (OIM), *J. Comput. Assist. Microscopy (USA)*, 1993, **5**, p 207–221.
50. A. Prakash, T.N. Tak, A. Lodh, N. Nayan, S.N. Murty, P. Guruprasad and I. Samajdar, Composition gradient and particle deformed zone: an emerging correlation, *Metall. Mater. Trans. A*, 2019, **50**(3), p 1250–1260.
51. B. Verlinden, J. Driver, I. Samajdar and R.D. Doherty, *Electron Backscatter Diffraction in Materials Science*, Springer, Berlin, 2009
52. H. Hwang and Y. Park, Effects of heat treatment on the phase ratio and corrosion resistance of duplex stainless steel, *Mater. Trans.*, 2009, **50**, p 0905110767–0905110767.
53. W.T. Tsai and J.R. Chen, Galvanic corrosion between the constituent phases in duplex stainless steel, *Corr. Sci.*, 2007, **49**(9), p 3659–3668.
54. Y.H. Yau and M. Streicher, Galvanic corrosion of duplex FeCr–10% Ni alloys in reducing acids, *Corrosion*, 1987, **43**(6), p 366–373.
55. E. Symmionis, Galvanic effects on the active dissolution of duplex stainless steels, *Corrosion*, 1990, **46**(1), p 2–12.
56. M. Khan, H. Mehtani, A. Durgaprasad, G. Goyal, M. Prasad, S. Parida, T. Dasgupta, N. Birbilis and I. Samajdar, The defining role of interface crystallography in corrosion of a two-phase pearlitic steel, *Phil. Mag.*, 2020, **100**, p 1439–1453.
57. T. Chandra, D. Bendeich and D. Dunne, *Dynamic Recovery and Recrystallization in a Duplex Stainless Steel*, *Strength of Metals and Alloys (ICSMA 6)*, Elsevier, London, 1982, p 505–510
58. L. Duprez, B. De Cooman and N. Akdut, Flow stress and ductility of duplex stainless steel during high-temperature torsion deformation, *Metall. Mater. Trans. A*, 2002, **33**(7), p 1931–1938.
59. A.A. Salem, S.R. Kalidindi and R.D. Doherty, Strain hardening of titanium: role of deformation twinning, *Acta Mater.*, 2003, **51**(14), p 4225–4237.
60. F.J. Humphreys and M. Hatherly, *Recrystallization and Related Annealing Phenomena*, Elsevier, London, 2012
61. H. McQueen, N. Ryan and E. Evangelista, Dynamic recrystallization in austenitic stainless steels, *Mater. Sci. Forum, Trans. Tech. Publ.*, 1993, **113**, p 435–440.
62. A. Dehghan-Manshadi and P.D. Hodgson, Dynamic recrystallization of austenitic stainless steel under multiple peak flow behaviours, *ISIJ Int.*, 2007, **47**(12), p 1799–1803.
63. K. Thool, K.M. Krishna, D. Srivastava, A. Patra, R. Doherty and I. Samajdar, Confirmation of dynamically recrystallized grains in hexagonal zirconium through local internal friction measurements, *Metall. Mater. Trans. A*, 2019, **50**(11), p 5000–5014.
64. P. Cizek, Microstructure evolution and softening processes in hot deformed austenitic and duplex stainless steels, *Mater. Sci. Forum, Trans. Tech. Publ.*, 2013, **753**, p 66–71.
65. A. Pinol-Juez, A. Iza-Mendia and I. Gutierrez,  $\delta/\gamma$  Interface boundary sliding as a mechanism for strain accommodation during hot deformation in a duplex stainless steel, *Metall. Mater. Trans. A*, 2000, **31**(6), p 1671–1677.
66. N. Haghdadadi, P. Cizek, H. Beladi, P.D. Hodgson, Hot deformation and restoration mechanisms in duplex stainless steels: Effect of strain rate, ESSC and DUPLEX 2017, 9th European Stainless Steel Conference-Science and Market and the 5<sup>th</sup> European Duplex Stainless Steel Conference and Exhibition, 2017, *Italian Association for Metallurgy*, p 5-16
67. J. Urcola and C. Sellars, Effect of changing strain rate on stress-strain behavior during high temperature deformation, *Acta Metall.*, 1987, **35**(11), p 2637–2647.

68. G. Fan, J. Liu, P. Han and G. Qiao, Hot ductility and microstructure in casted 2205 duplex stainless steels, *Mater. Sci. Eng. A*, 2009, **515**(1–2), p 108–112.
69. E. Evangelista, H. McQueen, M. Niewczas and M. Cabibbo, Hot workability of 2304 and 2205 duplex stainless steels, *Can. Metall. Q.*, 2004, **43**(3), p 339–353.
70. N. Haghdadi, D. Martin and P. Hodgson, Physically-based constitutive modelling of hot deformation behavior in a LDX 2101 duplex stainless steel, *Mater. Des.*, 2016, **106**, p 420–427.
71. D. Mukherjee, U. Tewary, S. Kumar, S. Karagadde, R. Verma, M. Sambandam and I. Samajdar, Imposed thermal gradients and resultant residual stresses: physical and numerical simulations, *Mater. Sci. Technol.*, 2020, **36**, p 1020–1036.
72. D.C. Sicupira, R.F. Assumpção, D.B. Perasoli, D.S. Alves, A.O.V. Ferreira and D.B. Santos, Effect of warm rolling on the corrosion and mechanical properties of UNS S32205 duplex stainless steel, *Mater. Res.*, 2019, **22**, p 1–12.
73. M. Seshweni, A. Moloto, S. Aribo, S. Oke, O. Ige and P. Olubambi, Influence of cold and hot rolling on the corrosion behaviour of duplex stainless steels in mine water environment, *Mater. Today Proc.*, 2020, **28**, p 912–915.

**Publisher's Note** Springer Nature remains neutral with regard to jurisdictional claims in published maps and institutional affiliations.